CrossMark

JM RAPIDS

Superconfined falling liquid films: linear versus nonlinear dynamics

Gianluca Lavalle[1], Sophie Mergui[2,3], Nicolas Grenier[4] and Georg F. Dietze[2],†

[1]Mines Saint-Etienne, Université Lyon, CNRS, UMR 5307 LGF, Centre SPIN, 42023 Saint-Etienne, France

[2]Université Paris-Saclay, CNRS, FAST, 91405 Orsay, France

[3]Faculté des Sciences et Ingénierie, Sorbonne Université, UFR d'Ingénierie, 75005 Paris, France

[4]Université Paris-Saclay, CNRS, LISN, 91405 Orsay, France

The effect of a counter-current gas flow on the linear stability of an inclined falling liquid film switches from destabilizing to stabilizing, as the flow confinement is increased. We confront this linear effect with the response of nonlinear surface waves resulting from long-wave interfacial instability. For the strongest confinement studied, the gas flow damps both the linear growth rate and the amplitude of nonlinear travelling waves, and this holds for waves of the most-amplified frequency and for low-frequency solitary waves. In the latter case, waves are shaped into elongated humps with a flat top that resist secondary instabilities. For intermediate confinement, the linear and nonlinear responses are opposed and can be non-monotonic. The linear growth rate of the most-amplified waves first decreases and then increases as the gas velocity is increased, whereas their nonlinear amplitude is first amplified and then damped. Conversely, solitary waves are amplified linearly but damped nonlinearly. For the weakest confinement, solitary waves are prone to two secondary instability modes that are not observed in unconfined falling films. The first involves waves of diminishing amplitude slipstreaming towards their growing leading neighbours. The second causes wave splitting events that lead to a train of smaller, shorter waves.

Key words: thin films, gas/liquid flow

1. Introduction

We consider a gravity-driven two-dimensional liquid film falling down a plane tilted at an angle ϕ with respect to the horizontal, in contact with a counter-current gas flow that is strongly confined by an upper wall placed at $y = H$ (figure 1). Both fluids are Newtonian,
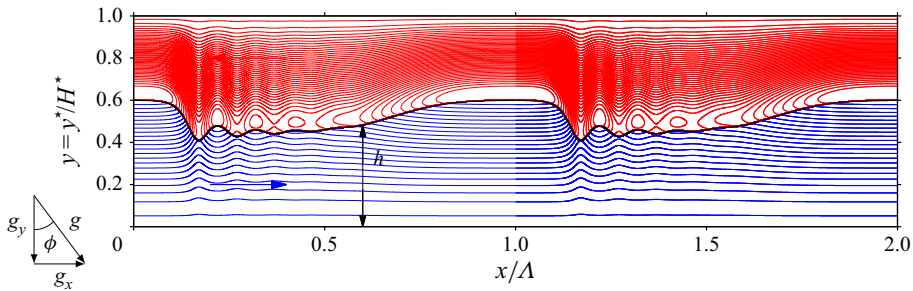
Figure 1. Problem sketch: gravity-driven falling liquid film (lower blue streamlines) in contact with a counter-current gas flow (upper red streamlines) flowing through a channel of dimensional gap height $H^\star$ inclined at an angle ϕ with respect to the horizontal. Streamlines (separated by constant streamfunction increments) are shown in the wall-fixed reference frame, and Λ is the wavelength.

with constant fluid properties, and the flow is laminar. Confined falling liquid films occur in rectification columns for cryogenic air separation, which contain structured packings that subdivide the column cross-section into millimetric channels (Valluri *et al.* 2005). Even stronger confinement is realized in compact reflux condensers (Vlachos *et al.* 2001), falling-film microreactors (Zhang *et al.* 2009) and micro-gap coolers (Kabov *et al.* 2011). We are interested in nonlinear waves that form on the surface of the falling liquid film due to the long-wave Kapitza instability (Kapitza 1948), and, in particular, how these are affected by the gas velocity in a strongly confined setting. Such waves are known to trigger flooding events, by local obstruction of the channel, by flow reversal or by wave reversal (Vlachos *et al.* 2001; Trifonov 2010*a*; Tseluiko & Kalliadasis 2011).

For weak confinements, flooding seems to be favoured by decreasing the gap height and/or increasing the gas flow rate. Experiments (Kofman, Mergui & Ruyer-Quil 2017) and numerical simulations (Trifonov 2010*a*,b) alike have shown that the amplitude of nonlinear waves increases with increasing counter-current gas flow, and that this growth diverges in the vicinity of the flooding point (Drosos, Paras & Karabelas 2006). Moreover, actual flooding experiments have shown that the critical gas flow rate decreases with diminishing gap height (Sudo 1996). Linear stability investigations, which demonstrate an increase in the maximal linear growth rate with increasing gas velocity, tend to confirm this nonlinear picture (Alekseenko *et al.* 2009; Vellingiri, Tseluiko & Kalliadasis 2015; Schmidt *et al.* 2016; Trifonov 2017).

On the other hand, recent investigations suggest that strong confinements may, in fact, lower the risk of flooding. Lavalle *et al.* (2019) have shown that the Kapitza instability can be entirely suppressed by sufficiently confining the gas, as suggested by Tilley, Davis & Bankoff (1994) and confirmed by Kushnir *et al.* (2021), and that this is facilitated by low tilt angles. Further, the authors observed that the linear stabilization, which they confirmed experimentally, is amplified by increasing the counter-current gas flow rate. Recent nonlinear direct numerical simulations (DNS) of inclined falling liquid films (Trifonov 2020) have identified a non-monotonic variation of the interfacial velocity, mean film thickness and inter-phase friction coefficient with increasing counter-current gas velocity, although the trend of the wave amplitude remained monotonic and increasing.

These investigations have motivated us to take a closer look at strongly confined *inclined* falling liquid films, in contrast to Dietze & Ruyer-Quil (2013) and Lavalle *et al.* (2020), who studied the vertical configuration, where the gas-induced linear stabilization is relatively weak. This is because the inertia-induced destabilizing mechanism of the Kapitza instability is weakened less and less by the stabilizing effect of normal gravity as

the tilt angle is increased, and thus the relative weight of the gas effect diminishes (Lavalle *et al.* 2019). We aim to confront linear stability predictions with the response of nonlinear surface waves to an increasingly strong counter-current gas flow. In particular, we wish to know whether nonlinear travelling waves can be damped under the effect of the gas flow, in line with the linear observations, and, if so, whether they may resist secondary instability. Such a situation would amount to a reduced flooding risk. By *secondary instability* we mean the loss of stability of travelling-wave solutions (TWS) produced by the primary Kapitza instability (Liu & Gollub 1993; Lavalle *et al.* 2020), and our analysis is restricted to two-dimensional such instability modes.

An enticing preliminary result was obtained by Samanta (2014), who showed that applying a constant interfacial shear stress to an inclined wavy falling liquid film can strongly reduce the amplitude of nonlinear surface waves. However, for the strong confinement studied here, variations of the shear stress with wave height play an important role (Lavalle *et al.* 2019), and the gas pressure gradient, which was also neglected in the model of Samanta (2014), needs to be accounted for (Dietze & Ruyer-Quil 2013).

To tackle this problem, we use the two-phase weighted residual integral boundary layer (WRIBL) model of Dietze & Ruyer-Quil (2013) to construct TWS, with the continuation software 'Auto07P' (Doedel 2008), and to compute spatially evolving wavy falling liquid films, with our own finite-difference code (Lavalle *et al.* 2020). These nonlinear computations are confronted with linear stability calculations based on the WRIBL model, and solutions of the full Orr–Sommerfeld (OS) eigenvalue problem (Tilley *et al.* 1994), whereby we have employed a spatial stability formulation (Barmak *et al.* 2016). Also, we check for periodic secondary instabilities via transient periodic computations started from TWS (Lavalle *et al.* 2020), and confront our model with a DNS based on the full Navier–Stokes equations, using the finite-volume solver 'Basilisk' (Popinet 2015).

Our paper is structured as follows. The mathematical description and numerical methods are introduced in § 2, followed by § 3, which reports results of our linear and nonlinear computations. Then, § 3.1 is dedicated to surface waves of the linearly most-amplified frequency, whereas § 3.2 concerns low-frequency solitary waves (here, we will also introduce our DNS data). Conclusions are drawn in § 4.

2. Mathematical description

The flow in figure 1 is governed by the Navier–Stokes and continuity equations, written in Einstein notation using the directional indices $i = 1, 2$ and $j = 1, 2$ ($x_1 = x$, $u_1 = u$, $x_2 = y$ and $u_2 = v$), and the phase indicator m, which identifies liquid ($m = l$) and gas ($m = g$):

$$X_m \partial_t u_i + u_j \partial_{x_j} u_i = -\partial_{x_i} p_m + Re_m^{-1} \partial_{x_j x_j} u_i + X_m^2 Fr^{-2} \{ \delta_{i1} \sin(\phi) - \delta_{i2} \cos(\phi) \}, \quad (2.1a)$$

$$\partial_{x_j} u_j = 0, \quad (2.1b)$$

where lengths have been scaled with the channel height $\mathcal{L} = H^\star$ (stars denote dimensional quantities throughout), velocities with the phase-specific signed superficial velocities $\mathcal{U}_m = q_{m0}^\star / H^\star$, time with $\mathcal{T} = \mathcal{L}/\mathcal{U}_l$, and the phase-specific pressure p_m with $\rho_m \mathcal{U}_m^2$. Further, δ_{ij} is the Kronecker symbol, $X_l = 1$ and $X_g = \mathcal{U}_l/\mathcal{U}_g$. The gravitational acceleration g enters through the Froude number $Fr = \mathcal{U}_l/\sqrt{g\mathcal{L}}$, and the Reynolds numbers $Re_m = \mathcal{U}_m \mathcal{L} (\rho_m/\mu_m) = q_{m0}^\star (\rho_m/\mu_m)$ are based on the phase-specific signed nominal flow rates $q_{m0}^\star$ of the flat-film primary flow, $q_{g0}^\star$ and Re_g being negative for a counter-current

gas flow. The boundary conditions are

$$u_l|_{y=0} = v_l|_{y=0} = u_g|_{y=1} = v_g|_{y=1} = 0, \tag{2.1c}$$

and the kinematic and dynamic coupling conditions at the film surface $y = h(x, t)$,

$$u_l = X_g^{-1} u_g, \quad v_l = X_g^{-1} v_g = \partial_t h + u_l \partial_x h, \tag{2.1d}$$

$$p_l + [S_{ij}^l n_j] n_i = X_g^{-2} \Pi_\rho p_g + X_g^{-1} \Pi_\mu [S_{ij}^g n_j] n_i + We \, \kappa, \tag{2.1e}$$

$$[S_{ij}^l n_j] \tau_i = X_g^{-1} \Pi_\mu [S_{ij}^g n_j] \tau_i, \tag{2.1f}$$

where $S_{ij}^m = \frac{1}{2}(\partial_{x_j} u_i + \partial_{x_i} u_j)$ denotes the strain-rate tensor, $\Pi_\mu = \mu_g/\mu_l$ and $\Pi_\rho = \rho_g/\rho_l$ are the dynamic viscosity and density ratios, and the surface tension σ enters through the Weber number $We = \sigma \rho_l^{-1} \mathcal{U}_l^{-2} \mathcal{L}^{-1}$. The orthonormal surface coordinate system is constructed by $\boldsymbol{n} = [-\partial_x h, 1](1 + \partial_x^2 h)^{-1/2}$ and $\boldsymbol{\tau} = [1, \partial_x h](1 + \partial_x^2 h)^{-1/2}$, from which we obtain the film surface curvature $\kappa = -\nabla \cdot \boldsymbol{n}$.

We perform two types of calculations based on the first principles (2.1) to validate our low-dimensional model. First, we solve the OS linear stability problem (Tilley *et al.* 1994), assuming spatially growing normal modes (Barmak *et al.* 2016):

$$\begin{bmatrix} h \\ \Phi \\ \Psi \\ p_m \end{bmatrix} = \begin{bmatrix} h_0 \\ \Phi_0(y) \\ \Psi_0(y) \\ p_{m0}(x, y) \end{bmatrix} + \begin{bmatrix} \hat{h} \\ \phi(y) \\ \psi(y) \\ \hat{p}_m(y) \end{bmatrix} \exp\{i(kx - \omega t)\}, \tag{2.2}$$

where Φ and Ψ designate the streamfunctions in the liquid and gas, the subscript 0 denotes the flat-interface base flow, $k \in \mathbb{C}$ is the complex wavenumber of the perturbation and $\omega \in \mathbb{R}$ is its angular frequency. We focus on long-wave instability modes, which we track through numerical continuation using Auto07P (Lavalle *et al.* 2019), having checked with a Chebyshev collocation code (Barmak *et al.* 2016) that short wave modes remain stable throughout the studied parameter range. Second, we perform a DNS with the finite-volume solver Basilisk (Popinet 2015), based on the volume-of-fluid (VOF) and the continuum surface force (CSF) methods, following (Dietze 2019). Here, we impose periodic conditions on a domain spanning the wavelength Λ.

Our low-dimensional model is based on the WRIBL approach (Ruyer-Quil & Manneville 1998; Kalliadasis *et al.* 2012), which describes the flow via evolution equations for the flow rate q and film height h. We employ the two-phase formulation of Dietze & Ruyer-Quil (2013) written in Einstein notation ($m = l, g$ and $n = l, g$):

$$\{S_m \partial_t q_m + F_{mn} q_m \partial_x q_n + G_{mn} q_j q_m \partial_x h\}$$
$$= -We \, \partial_{xxx} h + Fr^{-2}(1 - \Pi_\rho)\{\sin(\phi) - \cos(\phi)\partial_x h\} + Re_m^{-1} C_m q_m$$
$$+ Re_m^{-1}\{J_m q_m (\partial_x h)^2 + K_m \partial_x q_m \partial_x h + L_m q_m \partial_{xx} h + M_m \partial_{xx} q_m\}, \tag{2.3a}$$

$$\partial_x q_l + \partial_t h = 0, \quad \partial_x q_g - X_g \partial_t h = 0, \tag{2.3b}$$

where q_l and q_g denote the liquid and gas flow rates (per unit width) and the coefficients S_m, F_{mn}, G_{mn}, C_{mn}, J_n, K_n, L_n and M_n are known functions of the film height h (Dietze & Ruyer-Quil 2013).

We perform linear stability calculations by solving the dispersion equation $DR(\omega, k) = 0$, obtained by linearizing (2.3) around $[h_0, q_{l0}, q_{g0}]$, for $k = k_r + ik_i$ at a given $\omega \in \mathbb{R}$:

$$[h, q_l, q_g]^T = [h_0, q_{0l}, q_{0g}]^T + [\hat{h}, \hat{q}_l, \hat{q}_g]^T \exp\{i(kx - \omega t)\}, \qquad (2.4a)$$

$$DR = i\omega^2\{S_g - S_l\} + ik\omega\{F_{ml}q_m - F_{mg}q_m\} + ik^2 G_{mn}q_m q_n$$

$$+ ik^2 Fr^{-2}\{\cos(\phi) - \Pi_\rho \cos(\phi)\} - i^3 k^4 We + \omega\{Re_g^{-1}C_g - Re_l^{-1}C_l\}$$

$$- kRe_m^{-1}\partial_h C_m q_m - i^2 k^3 Re_m^{-1}L_m q_m + i^2 k^2 \omega\{Re_g^{-1}M_g - Re_l^{-1}M_l\}. \qquad (2.4b)$$

We also compute nonlinear TWS, which remain unaltered in a reference frame moving at the wave speed c, through numerical continuation based on (2.3), using Auto07P (Doedel 2008). Our code allows us to track TWS at the linearly most-amplified angular frequency $\omega = \omega_{max}$, via the following constraints (Dietze, Lavalle & Ruyer-Quil 2020):

$$DR(\omega_{max}, k) = 0, \quad \partial_\omega k_i|_{\omega = \omega_{max}} = 0. \qquad (2.5a,b)$$

Finally, we check the stability of nonlinear TWS via transient computations based on (2.3), using either periodic or inlet/outlet boundary conditions (Lavalle *et al.* 2020).

3. Results

We set the tilt angle to $\phi = 10°$ and focus on a single fluid combination, a 83 % by weight aqueous dimethylsulfoxide (DMSO) solution used in experiments (Dietze, Al-Sibai & Kneer 2009), where $\rho_l = 1098.3$ kg m^{-3}, $\mu_l = 3.13$ mPa s and $\sigma = 0.0484$ N m^{-1}, in contact with ambient air. The Kapitza number for this combination is $Ka = \sigma \rho_l^{-1/3} g^{-1/3} \mu_l^{-4/3} = 509.5$. The channel height $H^\star$ is varied as $H^\star = 1.2, 1.7, 1.8, 1.9,$ 2.1 and 2.4 mm, which corresponds to values of $\eta = 2, 2.8, 3, 3.1, 3.4$ and 3.9 for the relative confinement:

$$\eta = H^\star/h_0^\star|_{M=1} = 1/h_0|_{M=1}, \qquad (3.1)$$

where $h_0|_{M=1}$ is the primary flow film thickness for an aerostatic gas pressure gradient, i.e. $M = \partial_x p_g/\sin(\phi) = 1$. We wish to confront the linear and nonlinear implications of increasing the counter-current gas flow rate at fixed Re_l. In particular, we wish to know whether nonlinear waves can be damped via increasing $|Re_g|$.

3.1. *Most-amplified waves*

Figure 2 demonstrates the effect of increasing the counter-current gas flow rate on the linearly most-amplified waves ($\omega = \omega_{max}$) at fixed $Re_l = 15$ for different η values. Along each curve in figures 2(*a*) and 2(*c*), the channel height $H^\star$ remains fixed while h_0 increases (between 10 % for the strongest and 20 % for the weakest confinement), and so η (3.1) specifies a representative confinement for each case, corresponding to the rightmost point of each curve (where $M = 1$). Curves in figure 2(*a*) track the maximum linear spatial growth rate $-k_i^{max}$ in terms of Re_g, dashed lines corresponding to OS and solid lines to WRIBL calculations. At the largest η (filled squares, $\eta = 3.9$), the growth rate increases monotonically with $|Re_g|$, implying a gas-induced destabilization, up to the onset of absolute instability (AI), where $-k_{imax}$ diverges (Vellingiri *et al.* 2015). Conversely, at very small η values (open squares and pentagons, $\eta = 2, 2.8$), the effect of the gas is monotonically stabilizing, up to the point of fully suppressing (S) the long-wave Kapitza instability (Lavalle *et al.* 2019; Kushnir *et al.* 2021). In the intermediate range (crosses,
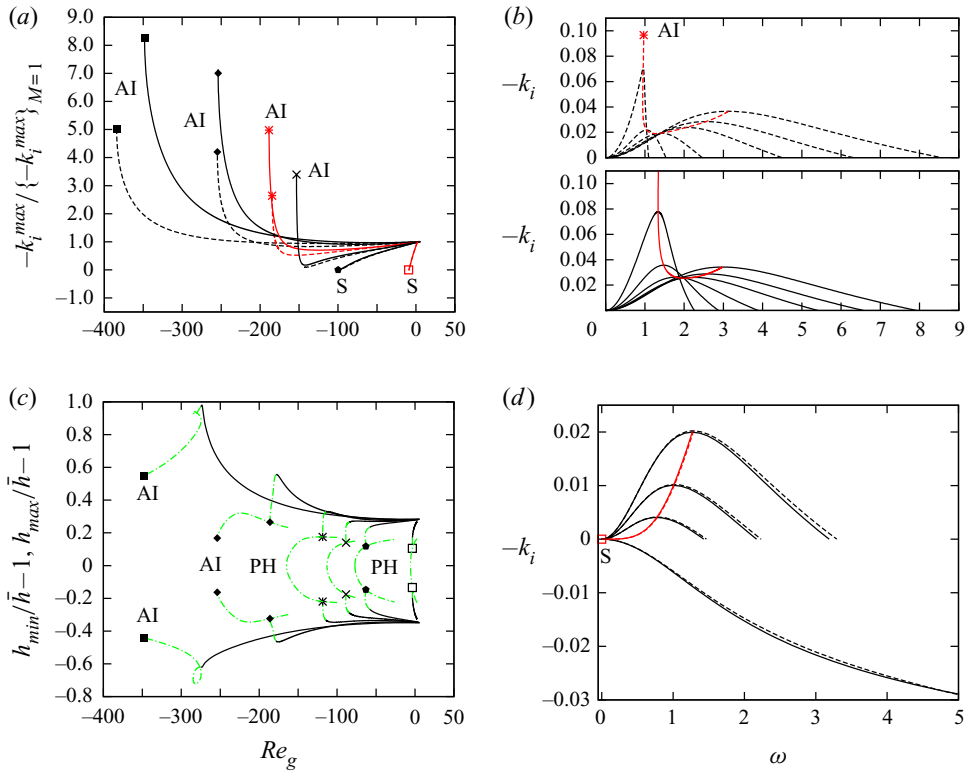
Figure 2. Most-amplified waves: $\phi = 10°$, $Re_l = 15$, $Ka = 509.5$. Linear (a,b,d) versus nonlinear (c) predictions. Filled squares, $\eta = 3.9$; diamonds, $\eta = 3.4$; asterisks, $\eta = 3.1$; crosses, $\eta = 3$; pentagons, $\eta = 2.8$; open squares, $\eta = 2$. (a) Maximal linear growth rate $-k_i^{max}$ versus Re_g, related to the aerostatic limit $\{-k_i^{max}\}_{M=1}$, where $M = \partial_x p_g / \sin(\phi)$. Solid, WRIBL; dashed, OS. (b,d) Dispersion curves $-k_i(\omega)$ for two cases from panel (a). Red curves trace $-k_i^{max}(\omega_{max})$ up to absolute instability (AI) or full stabilization (S). (b) For $\eta = 3.1$, from right to left: $M = 1$, $Re_g = -60, -100, -145, -170$ and -184. (d) For $\eta = 2$, from right to left: $M = 1$, $Re_g = -4, -7$ and -10. (c) Amplitude of nonlinear TWS (WRIBL) at $\omega = \omega_{max}$. PH denotes period-halving bifurcations and dot-dashed green lines identify periodically unstable TWS.

asterisks and diamonds, $\eta = 3, 3.1$ and 3.4), the behaviour is non-monotonic, stabilization occurring at low and destabilization at large values of $|Re_g|$. Figures 2(b) ($\eta = 3.1$) and 2(d) ($\eta = 2$) represent dispersion curves for the non-monotonic and fully stabilizing cases. Overall, there is quantitative agreement for $|Re_g| < 150$ between linear OS and WRIBL predictions in figures 2(a), 2(b) and 2(d), whereas qualitative agreement is retained when approaching the AI limits.

Figure 2(c) plots the upper and lower relative film height deflections $h_{max}/\bar{h} - 1$ and $h_{min}/\bar{h} - 1$ for nonlinear TWS at $\omega = \omega_{max}$, where $\bar{h} = \Lambda^{-1} \int_0^\Lambda h \, dx$ is the film height averaged over one wavelength, with $\bar{h} \neq h_0$ in the case of nonlinear waves. For $\eta = 3, 3.1$ and 3.4, TWS display a non-monotonic trend that is opposed to the linear one. That is, $h_{max}/\bar{h} - 1$ in figure 2(c), which we will refer to as the wave amplitude, first increases and then decreases with increasing $|Re_g|$, whereas $-k_i^{max}/\{-k_i^{max}\}_{M=1}$ in figure 2(a) first decreases and then increases. Conversely, for $\eta = 2$ and 2.8, the nonlinear and linear trends both imply stabilization, and, for $\eta = 3.9$, they both imply destabilization, at least up to the amplitude maximum in figure 2(c). Except for the two weakest confinements ($\eta = 2$,
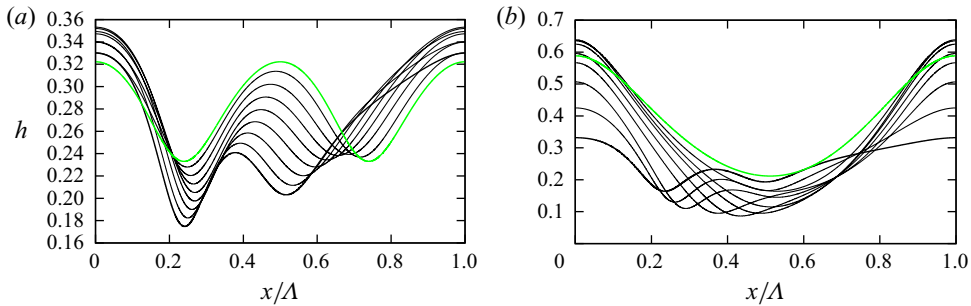
Figure 3. Wave profiles of TWS from figure 2(*c*). (*a*) For $\eta = 3$ (cross in figure 2*c*). Approaching the PH bifurcation: $Re_g = -37$ (thick solid) to $Re_g = -88$ (green). (*b*) For $\eta = 3.9$ (filled square in figure 2*c*). Suppression of the capillary ripple while approaching the AI limit: $Re_g = -79$ (thick solid) to $Re_g = -348$ (green).

2.8, 3 and 3.1), TWS are bounded by a nonlinear wave suppression, where $h_{max} = h_{min}$, resulting from period-halving (PH) bifurcations (marked by symbols), which sets in before the linear AI and S thresholds in figure 2(*a*). Figure 3(*a*) shows wave profiles leading up to such a PH bifurcation ($\eta = 3$). The sole precursory capillary ripple is seen to grow until splitting the wave into two identical halves. Conversely, for $\eta = 3.9$ (figure 3*b*), the capillary ripple disappears when increasing $|Re_g|$ towards the AI limit.

We conclude from figure 2 that linear stability predictions can be misleading. In particular, the amplitude of nonlinear waves may grow with increasing counter-current gas velocity, even though the linear growth rate decreases. Further, TWS become unstable to periodic secondary instability modes (dot-dashed lines in figure 2*c*) beyond a threshold Re_g, which we have determined via transient periodic computations started from TWS. These periodic modes do not lead to dangerous events, but TWS are also prone to a subharmonic instability in the case of a spatially evolving film (see supplementary movie 1 available at https://doi.org/10.1017/jfm.2021.417). Originally identified in unconfined films (Liu & Gollub 1993), this instability triggers wave coalescence events (Chang, Demekhin & Kalaidin 1996*a*) that can lead to intermittent flooding in long channels (Dietze & Ruyer-Quil 2013).

3.2. *Solitary waves*

We focus now on low-frequency solitary waves at a fixed wavelength $\Lambda = 4.5\tilde{\Lambda}_{max}$, where $\tilde{\Lambda}_{max}$ denotes the linearly most-amplified wavelength for a passive outer phase, all other parameters remaining as in figure 2. These waves lie on the ascending branch of the linear dispersion curves in figures 2(*b*) and 2(*d*), and thus the linear effect of increasing the gas flow is monotonic, either destabilizing ($\eta = 3, 3.1, 3.4$ and 3.9) or stabilizing ($\eta = 2$ and 2.8). Figure 4(*a*) represents the nonlinear response of solitary TWS, evidencing a monotonic gas-induced attenuation of the wave amplitude for $\eta = 2, 2.8, 3$ and 3.1. For $\eta = 3$ and 3.1, this nonlinear effect is opposed to the linear amplification, and both effects are inverted with respect to the initial response of the most-amplified waves (figure 2*a,c*). Solution branches of solitary TWS in figure 4(*a*) are bounded either by the linear thresholds of absolute instability (AI, $\eta = 3, 3.1$ and 3.4) and full stabilization (S, $\eta = 2$ and 2.8) from figure 2(*a*), or by a nonlinear limit point (LP, $\eta = 3.9$) that occurs slightly before (about 2 % in terms of Re_g) the AI bound.
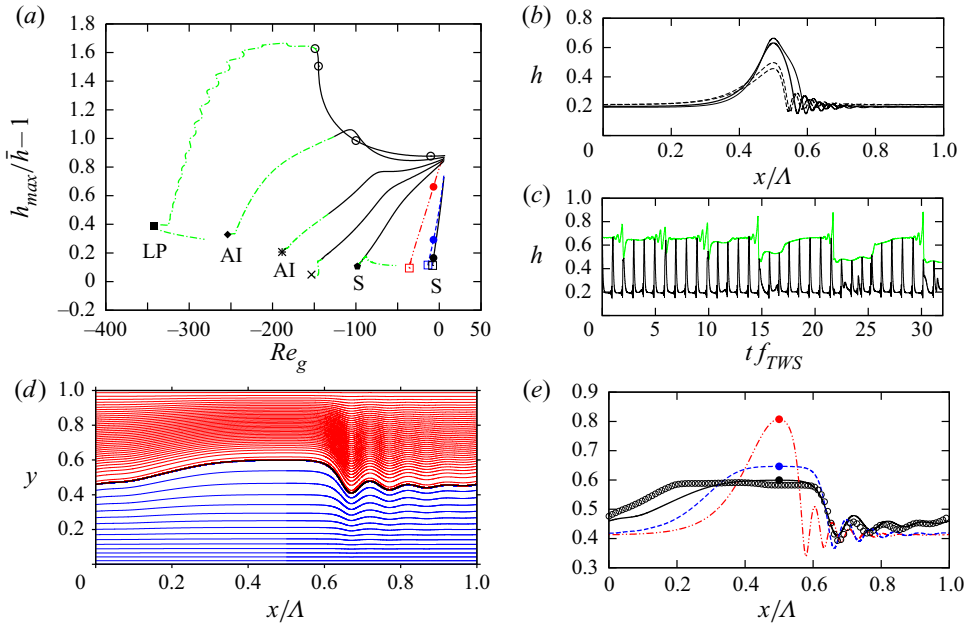
Figure 4. Solitary waves: $\phi = 10°$, $Re_l = 15$, $Ka = 509.5$, $\Lambda = 4.5\tilde{\Lambda}_{max}$. (*a*) Amplitude of nonlinear TWS (WRIBL). Right to left: $\eta = 2, 2$ ($\Pi_\mu = 0$), 2 ($\Pi_\rho = 0$), $2.8, 3, 3.1, 3.4$ and 3.9. Dot-dashed green lines highlight periodically unstable solutions. (*b*) Wave profiles corresponding to open circles ($\eta = 3.9$) in panel (*a*). Bottom to top: $Re_g = -10, -100, -145$ and -149. (*c*) Transient periodic computation started from thick-solid TWS in panel (*b*). Black, local film height; green, wave height. (*d*) Flat-top wave corresponding to black filled circle in figure 4(*a*): $\eta = 2$, $Re_g = -7$. Streamlines in the wave-fixed reference frame. (*e*) Different limits of the $\eta = 2$ solution in panel (*d*) (filled circles in panel *a*). Solid black, full inter-phase coupling; dashed blue, $\Pi_\mu = 0$ in (2.1*e*) and (2.1*f*); dot-dot-dashed red, $\Pi_\rho = 0$ in (2.1*e*); open circles, DNS at $M = \partial_x p_g / \sin(\phi) = M_{TWS} = 84.8$, $Re_l = 15.7$.

For the strongest confinement, $\eta = 2$ (open squares in figure 4*a*), linear and nonlinear effects are aligned and stabilizing. In that case, the gas shapes the wave hump into an elongated flat-top form (figure 4*d*). In figure 4(*e*), we compare this solution (solid line) with TWS in the limits $\Pi_\rho = 0$ (red dot-dot-dashed) and $\Pi_\mu = 0$ (blue dashed), which respectively deactivate the gas pressure and the gas-side viscous stresses in (2.1*e*) and (2.1*f*). From this comparison, we can conclude that the gas pressure gradient and not the gaseous viscous stresses are the cause for wave flattening. The flat-top TWS (also shown in figure 1), which we have reproduced with a DNS at slightly greater $Re_l = 15.7$ (open circles in figure 4*e*), is stable in periodic transient computations, and undergoes only weak modulations in a spatially evolving film (see supplementary movie 2).

For the weakest confinement, $\eta = 3.9$, solitary TWS are more susceptible to secondary instability modes. We discuss this based on the wave profiles in figure 4(*b*), which correspond to the TWS marked by open circles in figure 4(*a*). The TWS at $Re_g = -145$ (thick solid profile in figure 4*b*, second from left open circle in figure 4*a*) still lies on the periodically stable solution branch (solid curve in figure 4*a*). For this case, secondary instability can only arise through wave interactions. Pradas *et al.* (2013) showed, for the case of a passive atmosphere, that solitary waves can develop such interactions via the precursory capillary ripples, leading to oscillations around bound states, where neighbouring waves repeatedly approach and recoil from one another. Thereby, the approaching wave always grows, whereas the slowing wave always
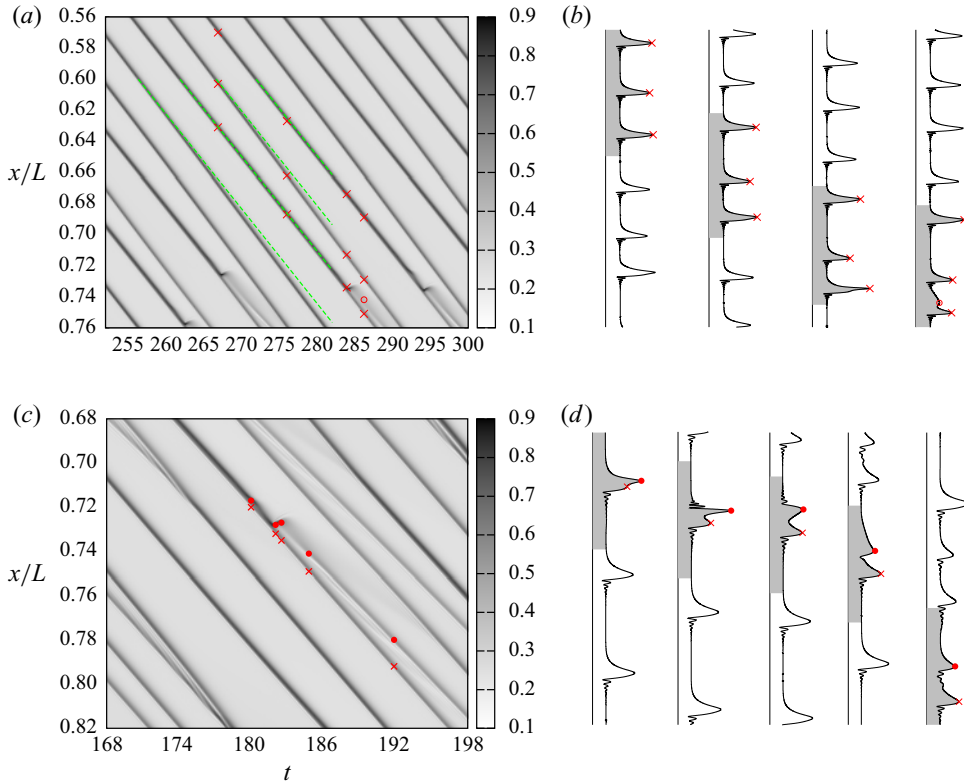
Figure 5. Slipstreaming (*a,b*) and wave splitting (*c,d*) in solitary wave trains. Spatio-temporal computations with our WRIBL model (2.3) on an open domain of length $L = 31.4\varLambda_{TWS}$, applying coherent inlet forcing at $f = f_{TWS}$: $\phi = 10°$, $\eta = 3.9$, $Re_l = 15$, $Ka = 509.5$. Space–time plots of the film height h (*a,c*), and wave profile snapshots (*b,d*). Parallel green dashed lines indicate initial TWS celerity. (*a,b*) For $Re_g = -145$, $f_{TWS} = 0.20$. (*c,d*) For $Re_g = -149$, $f_{TWS} = 0.19$. Red symbols identify primary/secondary wave maxima.

diminishes, in amplitude. In the presence of a counter-current gas flow, we observe a secondary instability mode that involves a different wave interaction. We demonstrate this through an open-domain computation with coherent inlet forcing at the TWS frequency $f = 2\pi/\omega = f_{TWS} = 0.20$. Figures 5(*a*) and 5(*b*) (see also supplementary movie 3) show that the instability produces solitary waves of diminishing amplitude that accelerate in the slipstream of their growing leading neighbours. This clearly differs from the behaviour of unconfined falling films, such as the above-mentioned oscillations around bound states (Pradas *et al.* 2013) or the well-known coarsening dynamics (Chang *et al.* 1996*b*), where larger-amplitude waves catch up with and accumulate the smaller ones travelling in front. The slipstreaming occurs in concert up- and downstream of a leading wave, and thus the latter is increasingly exposed to the counter-current gas flow, leading eventually to its destruction through a wave breaking event, before coalescence can occur.

When increasing the counter-current gas velocity further, TWS become periodically unstable (dot-dashed branches in figure 4*a*). For the TWS at $\eta = 3.9$ and $Re_g = -149$ (thin solid profile in figure 4*b*, leftmost open circle in figure 4*a*), the instability leads to a self-sustained repeated breaking and reconstructing of the wave crest, as shown in figure 4(*c*) via a transient computation with periodicity conditions started from the TWS. In a spatially evolving film, which we have mimicked through an

open-domain computation with inlet forcing frequency $f = f_{TWS} = 0.19$ (figure 5*c*,*d*, and see supplementary movie 4), the instability leads to ubiquitous wave splitting events that refine the solitary wave train into a train of shorter and smaller daughter waves. This gas-induced *refining dynamics* can be viewed as the opposite of the coarsening dynamics observed in unconfined films (Chang *et al.* 1996*b*). We point out that isolated wave splitting events have been observed in noise-driven wave regimes, both experimentally (Kofman *et al.* 2017) and numerically (Dietze & Ruyer-Quil 2013).

4. Conclusion

In this work, we have demonstrated that linear stability predictions of strongly confined falling liquid films can mislead in estimating the effect of a counter-current gas flow on the film's waviness. Both for waves of the most amplified frequency and for low-frequency solitary waves, we have identified situations where the linear and nonlinear responses are opposed, i.e. linear waves are damped while nonlinear ones are amplified, or *vice versa*. In some cases, linear waves are bounded by absolute instability, whereas nonlinear waves are fully suppressed via a period-halving bifurcation. Nonetheless, at very strong confinement, both the linear and nonlinear responses imply stabilization and TWS resist secondary instability. This suggests that the risk of wave-induced flooding can be lowered by strongly confining the flow. At weaker confinement, we have found two new secondary instability modes not observed in unconfined films. The first tends to coarsen the wave train, via smaller waves accelerating in the slipstream of their leading neighbours. The second causes wave splitting events that refine the wave train into a sequence of less dangerous shorter and smaller daughter waves.

Our two-dimensional analysis cannot account for the spanwise destabilization of TWS, which entails the formation of three-dimensional waves in the downstream portion of a spatially evolving falling liquid film (Chang 1994; Liu, Schneider & Gollub 1995; Scheid, Ruyer-Quil & Manneville 2006; Dietze *et al.* 2014; Kofman, Mergui & Ruyer-Qui 2014; Kharlamov *et al.* 2015). Nonetheless, we expect our conclusion on the stabilizing effect of strong confinement to extend to that situation. Firstly, the inertia-driven three-dimensional secondary instability mode (Kofman *et al.* 2014) is known to weaken at the small tilt angles considered here. In experiments, this translates to quasi-two-dimensional wave fronts with only weak spanwise modulations, which are maintained up to large gas velocities (Kofman *et al.* 2017). Secondly, the spanwise instability mode is dictated by the wall-normal acceleration of liquid within the initially two-dimensional wave hump. Thus, the gas effect on the amplitude of two- and three-dimensional wave humps is expected to be concurrent. This is supported by the weakly confined experiments of Kofman *et al.* (2017), where the counter-current gas flow amplified both instability modes. In our strongly confined setting, we expect the opposite, i.e. a damping of both modes.

The channel heights considered here (1.2 mm $\leq H^{\star} \leq$ 2.4 mm) lie in between the range of classical (Vlachos *et al.* 2001) falling-film experiments ($H^{\star} \geq 5$ mm) and microchannel (Zhang *et al.* 2009; Hu & Cubaud 2018) falling-film experiments ($H^{\star} \leq 1$ mm). Also, strongly confined experiments have generally not considered small tilt angles. Our numerical computations suggest that this uncharted part of the regime map deserves experimental attention. Should experiments confirm our findings, it would mean that surface waves can be maintained in very compact liquid/gas exchangers without the risk of flooding. Current microreactor designs consist of arrays of narrow grooves, where the film surface is pinned laterally (Al-Rawashdeh *et al.* 2008), and this effectively suppresses surface waves (Pollak, Haas & Aksel 2011), solving the flooding problem, but at the cost of waiving the substantial wave-induced intensification of heat/mass transfer (Yoshimura,

Nosoko & Nagata 1996). Our results suggest relaxing the lateral confinement in such devices to allow for the development of surface waves. Experiments in horizontal wavy liquid-film/gas flows through mini-gaps (Kabov *et al.* 2007, 2011) have shown that it is possible to produce the strong crosswise confinement levels studied here ($H^\star = 2$ mm) at weak spanwise confinement ($W^\star = 40$ mm).

Author ORCIDs.
Gianluca Lavalle https://orcid.org/0000-0002-9866-5216;
Georg F. Dietze https://orcid.org/0000-0003-1495-5505.

REFERENCES

AL-RAWASHDEH, M., HESSEL, V., LÖB, P., MEVISSEN, K. & SCHÖNFELD, F. 2008 Pseudo 3-d simulation of a falling film microreactor based on realistic channel and film profiles. *Chem. Engng Sci.* **63**, 5149–5159.

ALEKSEENKO, S.V., AKTERSHEV, S.P., CHERDANTSEV, A.V., KHARLAMOV, S.M. & MARKOVICH, D.M. 2009 Primary instabilities of liquid film flow sheared by turbulent gas stream. *Intl J. Multiphase Flow* **35**, 617–627.

BARMAK, I., GELFGAT, A., VITOSHKIN, H., ULLMAN, A. & BRAUNER, N. 2016 Stability of stratified two-phase flows in horizontal channels. *Phys. Fluids* **28**, 044101.

CHANG, H.C. 1994 Wave evolution on a falling film. *Annu. Rev. Fluid Mech.* **26**, 103–136.

CHANG, H.C., DEMEKHIN, E.A. & KALAIDIN, E. 1996*a* Simulation of noise-driven wave dynamics on a falling film. *AIChE J.* **42** (6), 1553–1568.

CHANG, H.C., DEMEKHIN, E.A., KALAIDIN, E. & YE, Y. 1996*b* Coarsening dynamics of falling-film solitary waves. *Phys. Rev.* E **54** (2), 1467–1477.

DIETZE, G.F. 2019 Effect of wall corrugations on scalar transfer to a wavy falling liquid film. *J. Fluid Mech.* **859**, 1098–1128.

DIETZE, G.F., AL-SIBAI, F. & KNEER, R. 2009 Experimental study of flow separation in laminar falling liquid films. *J. Fluid Mech.* **637**, 73–104.

DIETZE, G.F., LAVALLE, G. & RUYER-QUIL, C. 2020 Falling liquid films in narrow tubes: occlusion scenarios. *J. Fluid Mech.* **894**, A17.

DIETZE, G.F., ROHLFS, W., NÄHRICH, K., KNEER, R. & SCHEID, B. 2014 Three-dimensional flow structures in laminar falling liquid films. *J. Fluid Mech.* **743**, 75–123.

DIETZE, G.F. & RUYER-QUIL, C. 2013 Wavy liquid films in interaction with a confined laminar gas flow. *J. Fluid Mech.* **722**, 348–393.

DOEDEL, E.J. 2008 *AUTO07p: continuation and bifurcation software for ordinary differential equations.* Montreal Concordia University.

DROSOS, E.I.P., PARAS, S.V. & KARABELAS, A.J. 2006 Counter-current gas-liquid flow in a vertical narrow channel - liquid film characteristics and flooding phenomena. *Intl J. Multiphase Flow* **32**, 51–81.

HU, X. & CUBAUD, T. 2018 Viscous wave breaking and ligament formation in microfluidic systems. *Phys. Rev. Lett.* **121**, 044502.

KABOV, O.A., LYULIN, Y.. V., MARCHUK, I.V. & ZAITSEV, D.V. 2007 Locally heated shear-driven liquid films in microchannels and minichannels. *Intl J. Heat Fluid Flow* **28**, 103–112.

KABOV, O.A., ZAITSEV, D.V., CHEVERDA, V.V. & BAR-COHEN, A. 2011 Evaporation and flow dynamics of thin, shear-driven liquid films in microgap channels. *Exp. Therm. Fluid Sci.* **35**, 825–831.

KALLIADASIS, S., RUYER-QUIL, C., SCHEID, B. & VELARDE, M.G. 2012 *Falling Liquid Films*, Applied Mathematical Sciences, vol. 176. Springer Verlag.

KAPITZA, P.L. 1948 Wave flow of thin layer of viscous fluid (in Russian). *Zhurn. Eksper. Teor. Fiz.* **18** (1), 3–28.

KHARLAMOV, S.M., GUZANOV, V.V., BOBYLEV, A.V., ALEKSEENKO, S.V. & MARKOVICH, D.M. 2015 The transition from two-dimensional to three-dimensional waves in falling liquid films: wave patterns and transverse redistribution of local flow rates. *Phys. Fluids* **27**, 114106.

KOFMAN, N., MERGUI, S. & RUYER-QUI, C. 2014 Three-dimensional instabilities of quasi-solitary waves in a falling liquid film. *J. Fluid Mech.* **757**, 854–887.

KOFMAN, N., MERGUI, S. & RUYER-QUIL, C. 2017 Characteristics of solitary waves on a falling liquid film sheared by a turbulent counter-current gas flow. *Intl J. Multiphase Flow* **95**, 22–34.

KUSHNIR, R., BARMAK, I., ULLMANN, A. & BRAUNER, N. 2021 Stability of gravity-driven thin-film flow in the presence of an adjacent gas phase. *Intl J. Multiphase Flow* **135**, 103443.

LAVALLE, G., GRENIER, N., MERGUI, S. & DIETZE, G.F. 2020 Solitary waves on superconfined falling liquid films. *Phys. Rev. Fluids* **5** (3), 032001(R).

LAVALLE, G., LI, Y., MERGUI, S., GRENIER, N. & DIETZE, G.F. 2019 Suppression of the kapitza instability in confined falling liquid films. *J. Fluid Mech.* **860**, 608–639.

LIU, J. & GOLLUB, J.P. 1993 Onset of spatially chaotic waves on flowing films. *Phys. Rev. Lett.* **70** (15), 2289–2292.

LIU, J., SCHNEIDER, J.B. & GOLLUB, J.P. 1995 Three-dimensional instabilities of film flows. *Phys. Fluids* **7** (1), 55–67.

POLLAK, T., HAAS, A. & AKSEL, N. 2011 Side wall effects on the instability of thin gravity-driven films - from long-wave to short-wave instability. *Phys. Fluids* **23**, 094110.

POPINET, S. 2015 A quadtree-adaptive multigrid solver for the serre-green-naghdi equations. *J. Comput. Phys.* **302**, 336–358.

PRADAS, M., KALLIADASIS, S., NGUYEN, P.-K. & BONTOZOGLOU, V. 2013 Bound-state formation in interfacial turbulence: direct numerical simulations and theory. *J. Fluid Mech.* **716**, R2.

RUYER-QUIL, C. & MANNEVILLE, P. 1998 Modeling film flows down inclined planes. *Eur. Phys. J.* B **6** (2), 277–292.

SAMANTA, A. 2014 Shear-imposed falling film. *J. Fluid Mech.* **753**, 131–149.

SCHEID, B., RUYER-QUIL, C. & MANNEVILLE, P. 2006 Wave patterns in film flows: modelling and three-dimensional waves. *J. Fluid Mech.* **562**, 183–222.

SCHMIDT, P., NÁRAIGH, L.Ó., LUCQUIAUD, M. & VALLURI, P. 2016 Linear and nonlinear instability in vertical counter-current laminar gas-liquid flows. *Phys. Fluids* **28**, 042102.

SUDO, Y. 1996 Mechanism and effects of predominant parameters regarding limitation of falling water in vertical countercurrent two-phase flow. *J. Heat Transfer* **118** (3), 715–724.

TILLEY, B.S., DAVIS, S.H. & BANKOFF, S.G. 1994 Linear stability theory of two-layer fluid flow in an inclined channel. *Phys. Fluids* **6** (12), 3906–3922.

TRIFONOV, Y.Y. 2010*a* Counter-current gas-liquid wavy film flow between the vertical plates analyzed using the Navier–Stokes equations. *AIChE J.* **56** (8), 1975–1987.

TRIFONOV, Y.Y. 2010*b* Flooding in two-phase counter-current flows: numerical investigation of the gas-liquid wavy interface using the Navier–Stokes equations. *Intl J. Multiphase Flow* **36**, 549–557.

TRIFONOV, Y.Y. 2017 Instabilities of a gas-liquid flow between two inclined plates analyzed using the Navier–Stokes equations. *Intl J. Multiphase Flow* **95**, 144–154.

TRIFONOV, Y.Y. 2020 Linear and nonlinear instabilities of a co-current gas-liquid flow between two inclined plates analyzed using the Navier–Stokes equations. *Intl J. Multiphase Flow* **122**, 103159.

TSELUIKO, D. & KALLIADASIS, S. 2011 Nonlinear waves in counter-current gas-liquid film flow. *J. Fluid Mech.* **673**, 19–59.

VALLURI, P., MATAR, O.K., HEWITT, G.F. & MENDES, M.A. 2005 Thin film flow over structured packings at moderate Reynolds numbers. *Chem. Engng Sci.* **60**, 1965–1975.

VELLINGIRI, R., TSELUIKO, D. & KALLIADASIS, S. 2015 Absolute and convective instabilities in counter-current gas-liquid film flows. *J. Fluid Mech.* **763**, 166–201.

VLACHOS, N.A., PARAS, S.V., MOUZA, A.A. & KARABELAS, A.J. 2001 Visual observations of flooding in narrow rectangular channels. *Intl J. Multiphase Flow* **27**, 1415–1430.

YOSHIMURA, P.N., NOSOKO, P. & NAGATA, T. 1996 Enhancement of mass transfer into a falling laminar liquid film by two-dimensional surface waves-some experimental observations and modeling. *Chem. Engng Sci.* **51** (8), 1231–1240.

ZHANG, H., CHEN, G., YUE, J. & YUAN, Q. 2009 Hydrodynamics and mass transfer of gas-liquid flow in a falling film microreactor. *AIChE J.* **55** (5), 1110–1120.